Exciton decay mechanism in DNA single strands:
back-electron transfer and ultrafast base motions

Benjamin Bauer[1]**, Rahul Sharma**[2]**, Majed Chergui**[1]**, and Malte Oppermann***[1]

[1]Laboratoire de Spectroscopie Ultrarapide and LACUS, École Polytechnique Fédérale de Lausanne, ISIC-FSB, CH-1015 Lausanne, Switzerland
[2]Laboratory for Computation and Visualization in Mathematics and Mechanics, École Polytechnique Fédérale de Lausanne, MATH-FSB, CH-1015 Lausanne, Switzerland

*malte.oppermann@epfl.ch

Supplementary Information

This supplementary information provides technical details concerning the performed experiments and their analysis. In the first section, the steady-state absorption and circular dichroism spectra of the investigated samples are displayed. In the second section, the two-photon absorption signal in a neat buffer solution is presented in order to assess the time-resolution of the presented experiments. In the third and fourth sections, the data analysis and fitting procedures for the transient absorption (TA), respectively anisotropy (TAA) measurements are discussed and evaluated.

1 Steady-state spectra
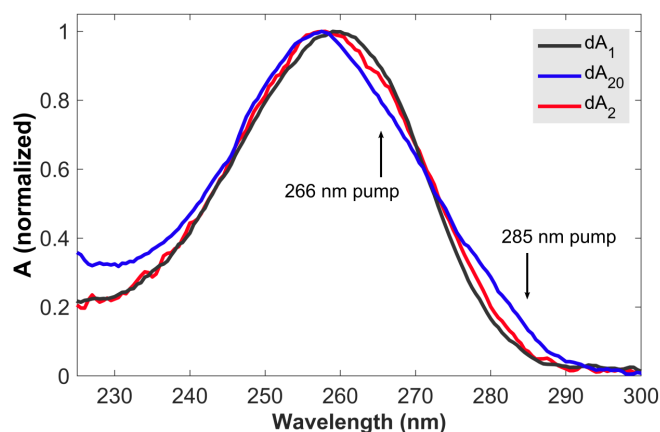
Figure 1. Steady-state absorption spectra of dA_1, dA_{20}, and dA_2 in aqueous phosphate buffer solution, each normalized to its absorption maximum. The spectral differences illustrate the impact of dipole-dipole and charge transfer interactions between the adenosine bases.
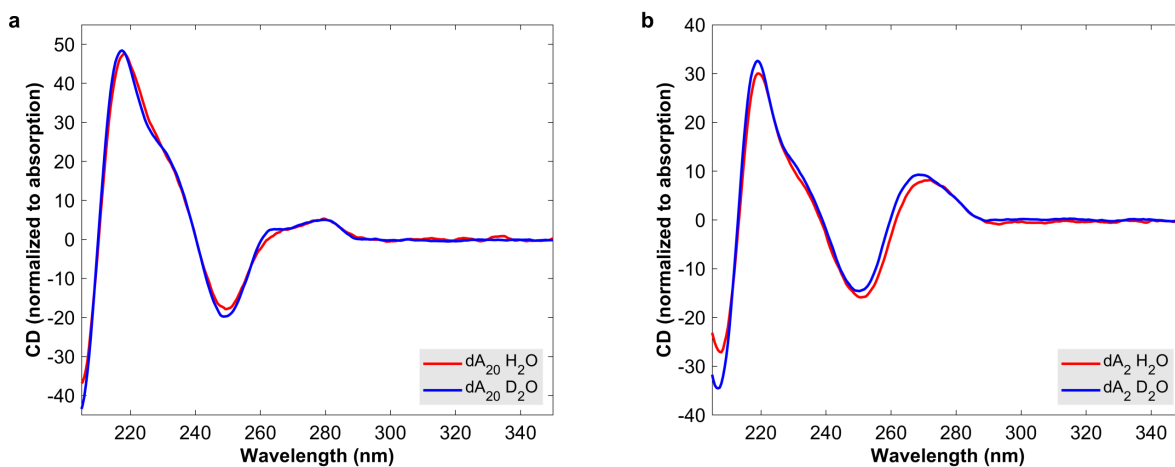
Figure 2. a) Circular dichroism (CD) spectra of dA_{20} in H_2O and D_2O buffer solution. To account for possible solvent impacts on the absorption coefficient, the CD spectra are normalized to the absorption maximum near 260 nm for each sample. **b)** CD spectra of dA_{20} in H_2O and D_2O buffer solution with the same normalization procedure.

2 Two-photon absorption in buffer solution

In order to determine the instrument response function (IRF) of the TA and TAA measurements presented in the main text, the nonlinear response of the neat solvent at pump-probe overlap was recorded. Here, the employed pump fluence of appoximately 300 μJ cm^{-2} was more than doubled compared to the presented sample measurements, in order to achieve a good signal-to-noise. The TA is displayed as a time-wavelength map in fig. 3a, which shows a parabolic pump-probe delay dependence of the temporal overlap of the spectral components of the probe pulse. This effect is caused by the probe pulse's group
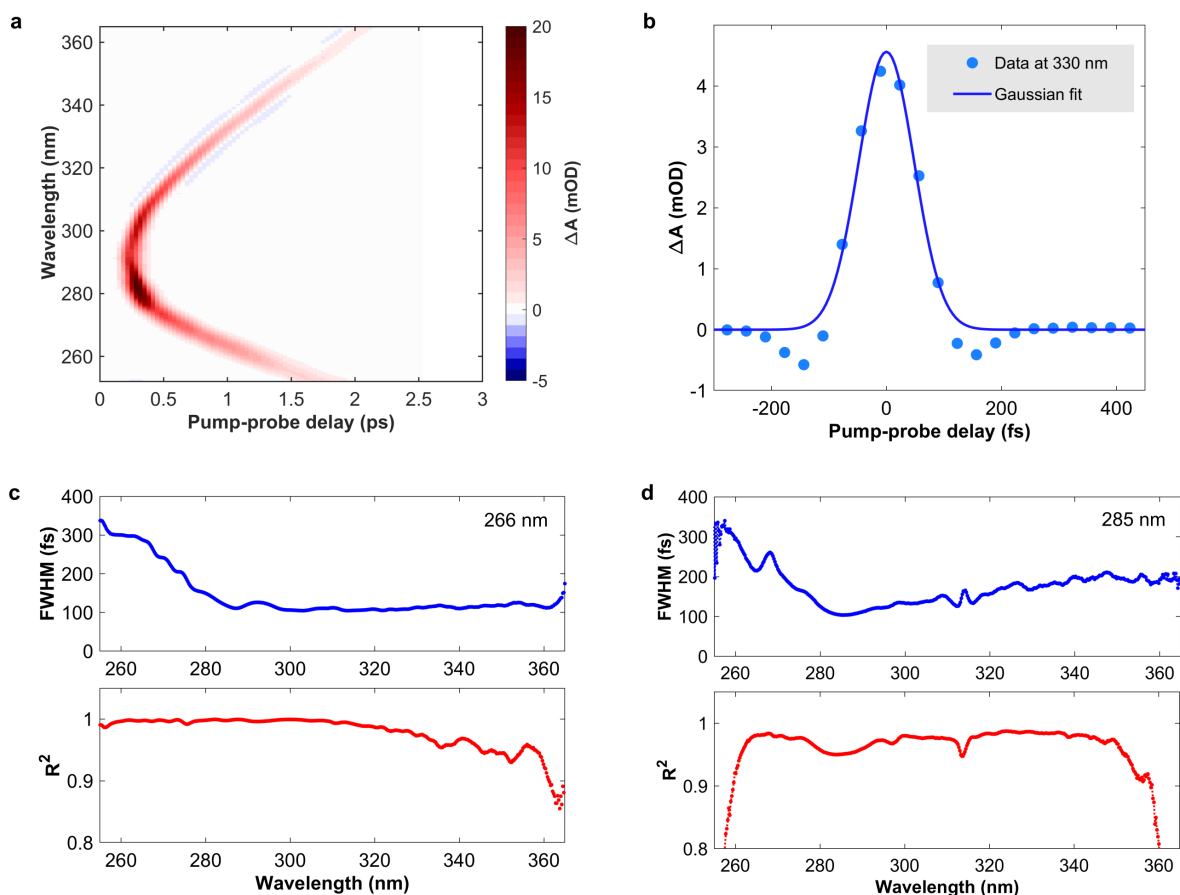
Figure 3. a) displays the transient absorption time-wavelength map of a neat H_2O buffer solution excited with a pump pulse centred at 266 nm and with an estimated fluence of 300 $\mu J\ cm^{-2}$. The nonlinear solvent response is dominated by two-photon absorption during the temporal overlap of the pump and probe pulses, which can be fitted with a Gaussian function. **b)** Kinetic trace obtained from (a) at a probe wavelength of 330 nm and the corresponding Gaussian fit. **c)** Full-width at half maximum (FWHM) of the performed Gaussian fits as a function of probe wavelength and the associated R^2 value obtained for each fit for a 266 nm pump pulse. The obtained FWHM correspond to the instrument response function (IRF) quoted in the main text. **d)** FWHM and fit quality obtained for a 285 nm pump pulse.

velocity dispersion (GVD), which is routinely corrected in the post-processing of transient absorption data. Fig. 3a shows an exemplary time trace taken from the time-wavelength map at 330 nm. It shows that the solvent response is dominated by a strong positive signal mostly caused by two-photon absorption from the pump and probe pulses. There is an additional minor negative signal contribution that is caused by cross-phase modulation. The IRF is estimated as the full-width at half maximum (FWHM) from a Gaussian function fitted to the individual time traces at each probe wavelength. The resulting FWHM values as a function of the probe wavelength are displayed in fig. 3c,d, for pump pulses centered at 266 nm and 285 nm respectively, along with the associated R^2 value. Whilst the IRF is <150 fs in the spectral region >280 nm, it increases to about 350 fs for shorter wavelengths. This is most likely caused by the increase in dispersion for shorter wavelengths in commonly employed optical materials. In this context, it

should be noted that fig. 3b illustrates that the shortest time-delay that can be probed without any signal from the solvent is approximately 250 fs from the centre of two-photon absorption signal.

3 Transient absorption

Before any global fits were performed, the time-wavelength TA maps were GVD corrected, making use of the prominent two-photon absorption signal at pump-probe overlap. As the main concern of the analysis is to extract the dynamics of the charge-transfer (CT) exciton on the picosecond time scale, data points below 0.4 picoseconds were disregarded, thereby excluding contributions from two-photon absorption and cross-phase modulation near the pump-probe overlap. As a consequence, kinetics on the sub-picosecond time scale were not resolved in the quantitative analysis. The TA data was fitted with a sequence of exponential decays convoluted with a Gaussian IRF, using the OPTIMUS software package[1]. In all cases, the minimum number of exponential decays to achieve a suitable fit was applied, as explained in the main text. Fig. 4 displays the time-wavelength TA maps, the obtained decay associated spectra (DAS) for dA_1 (266 nm), dA_2 (266 nm), and dA_{20} (266 nm) in H_2O buffer solution. To evaluate the quality of the global fits, fig. 5 displays the associated time-wavelength maps of the obtained residuals and time traces of the TA amplitude, which compare the fit to the data points at selected probe wavelengths. Fig. 6 and 7 then show the same information for these samples in D_2O buffer solution, whereas fig. 9 displays the results for dA_{20} (285 nm) in H_2O buffer solution. Note that dA_{20} (285 nm) displays a particularly low signal amplitude due to the low absorption coefficient at the excitation wavelength of 285 nm. To achieve a good signal-to-noise, the number of sampled pump-probe delays was reduced to accumulate a higher number of pump-probe scans.

In the case of dA_1 (266 nm) in H_2O, two exponential decays were required to achieve an appropriate fit quality, accounting for the observed spectral shifts. The corresponding residuals are highest in the spectral range which is dominated by vibrational cooling dynamics and at most around 2%. This is consistent with the well-known observation that spectral shifts cannot be modeled quantitatively by global multi-exponential fits. However, for the presented analysis the achieved fit quality is sufficient to describe the kinetics of the vibrational cooling dynamics without distorting the TA kinetics on longer time scales. In particular, the exciton relaxation dynamics in dA_2 (266 nm) and dA_{20} (266 nm) take place on time scales that are two orders of magnitude slower. Following previously published results on the relaxation kinetics in dA_n[2,3], two decay components were added to the exponential decay sequence in A_2 (266 nm) and dA_{20} (266 nm): a component on the 100 ps scale describing the relaxation of the CT exciton and a component with a time constant »1 ns accounting for long-lived radical species[4]. We achieve a very good fit quality with low residuals, which are <1% across the probed spectral range for pump-probe delays >10 ps. Here, the lowest residuals are achieved for dA_{20}, because it displays negligible vibrational cooling dynamics as explained in the main text. Due to the high quality of the global fits, we assign a 10% error to each of the obtained decay constants. To avoid any over-fitting of the data and corroborate the choice of four

exponential decay components, we took dA_2 as an exemplary case and removed exponential components from the global fit in a step-wise fashion. Fig. 8 then compares the residuals and time traces for global fits with four, three and two components. Removing the longest decay component τ_4 (fig. 8b,e) results in significantly larger residuals >100 ps, whereas the additional removal of the sub-picosecond component τ_1 leads to a global mismatch between the data and the fits (fig. 8c,d). This confirms that four decay components are required to achieve an adequate fit of the oligomer data sets.

For the samples in D_2O buffer solution comparable fit qualities are obtained, as is visualized by the low residuals. However, the solvent deuteration has a significant impact on the observed TA kinetics. Whilst slower vibrational cooling dynamics are already observed in dA_1, A_2 and dA_{20} also display a much longer CT exciton relaxation time. Finally, the fits obtained for dA_{20} (285 nm) in H_2O buffer solution show a similar quality as the previously discussed samples.
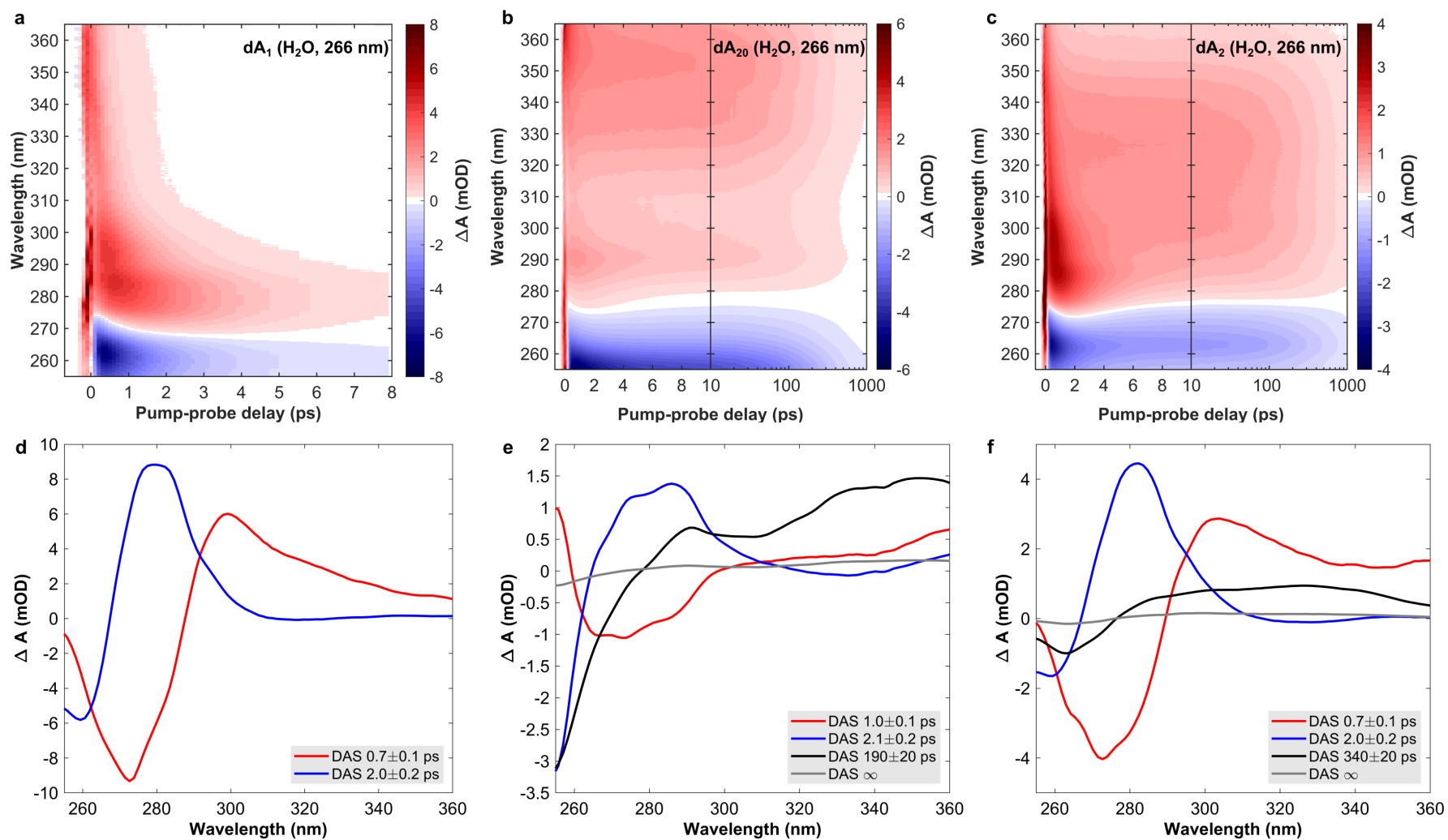
Figure 4. a,b,c) Time-wavelength TA maps for dA_1, dA_{20}, and dA_2, respectively, in H_2O buffer solution, photoexcited at 266 nm. **d,e,f)** DAS obtained from global fits of the respective data sets (a,b,c), where a sequence of multiexponential decays convoluted with the experiment's instrument response function was employed as the fit function.
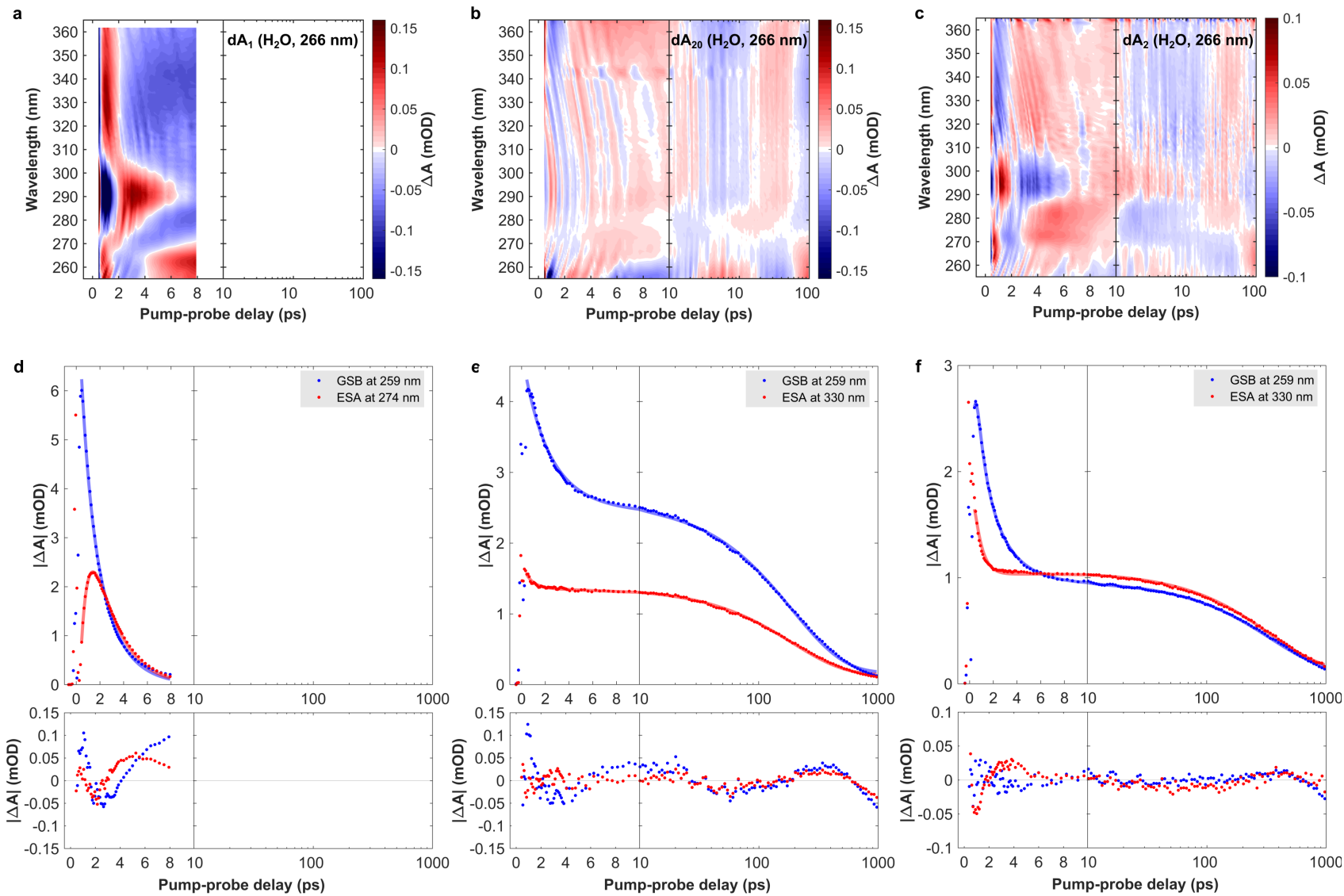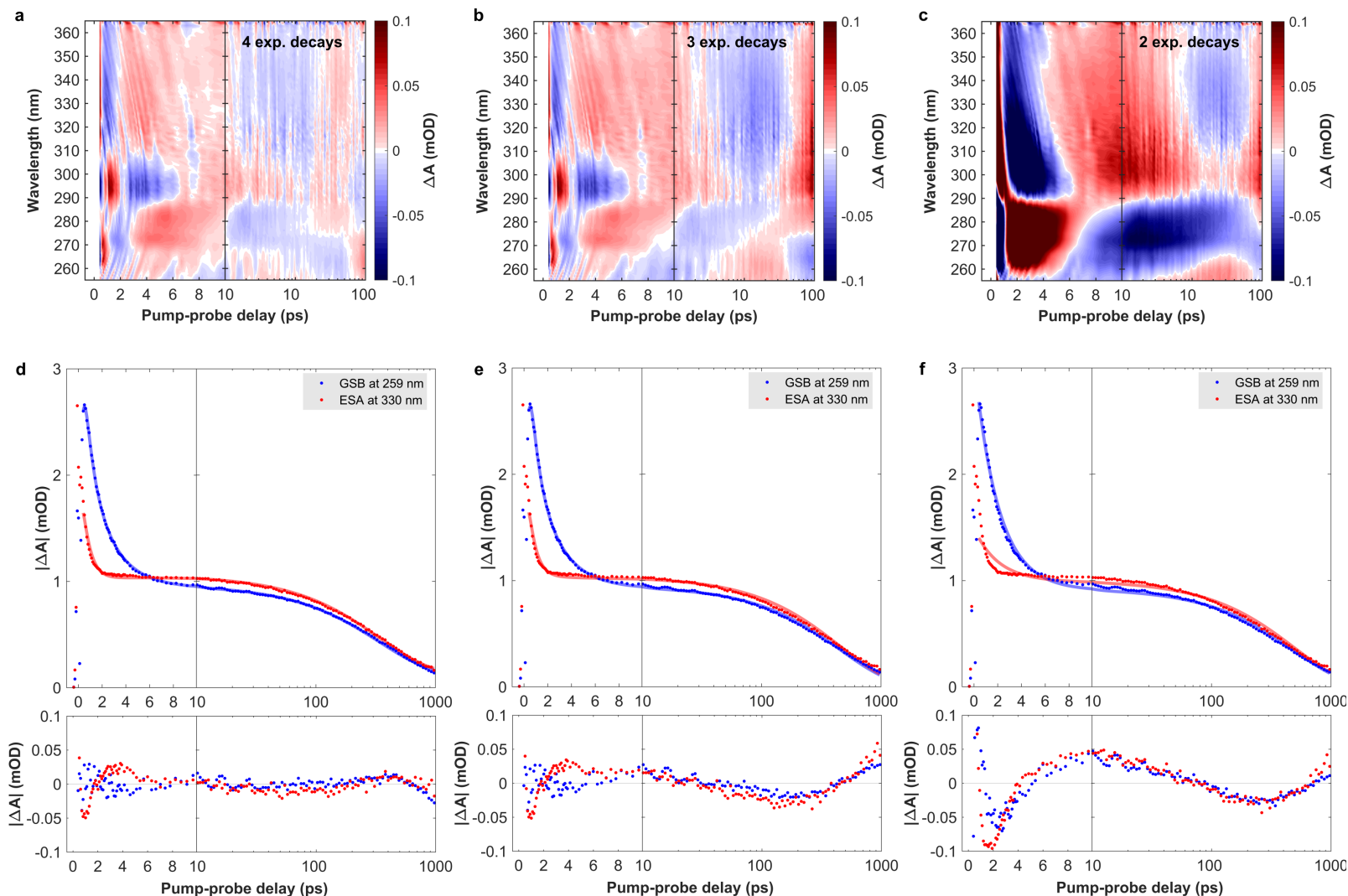
Figure 5. a,b,c) Time-wavelength maps of the residuals obtained from the fits performed on the respective data sets displayed in fig. 4. **d,e,f)** Absolute value of the TA amplitude as a function of pump-probe delay for selected probe wavelengths. Measured data points are displayed as dots and the multi-exponential fits as solid lines. The associated fit residuals are displayed in the lower panel.
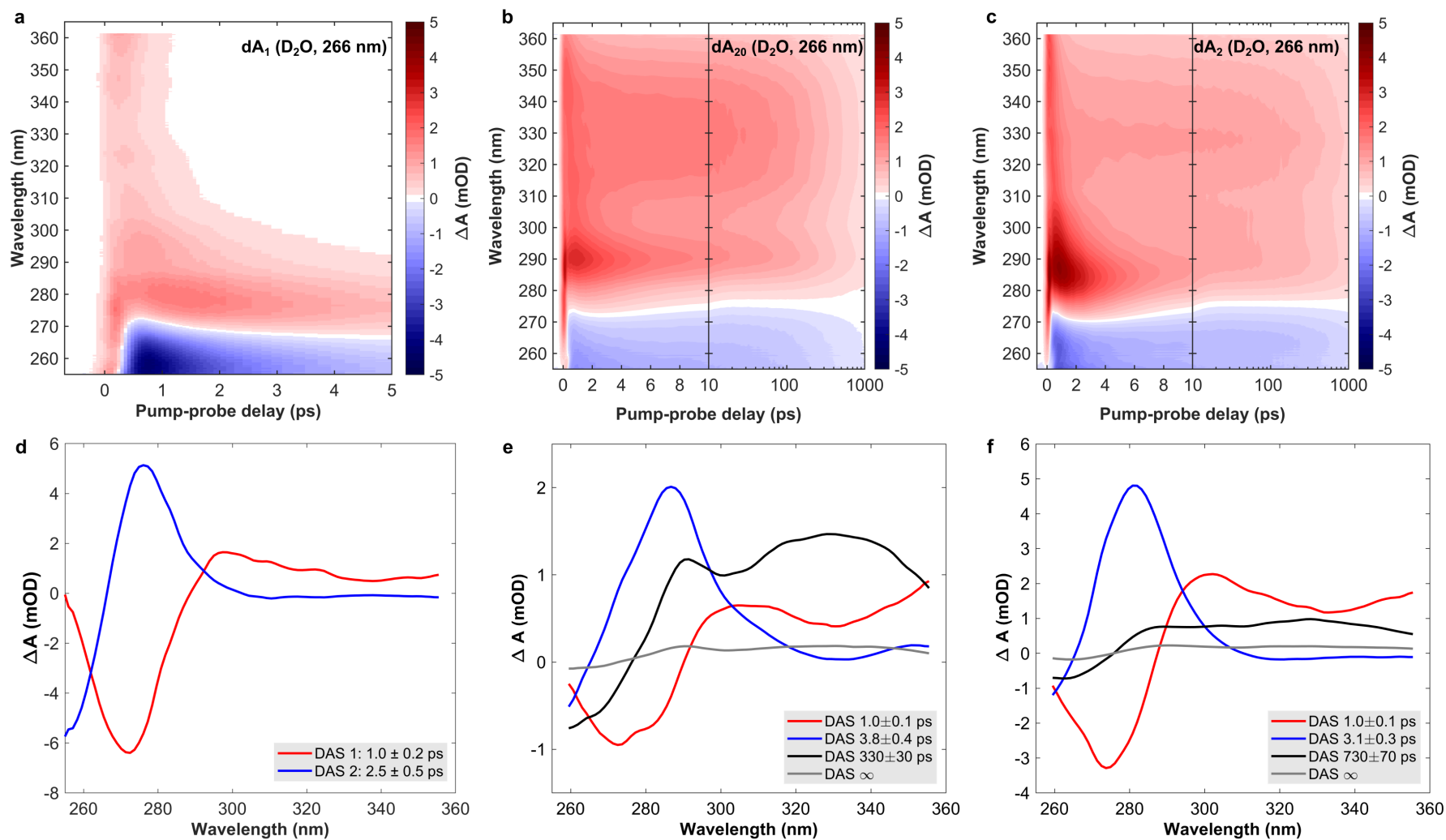
Figure 6. a,b,c) Time-wavelength TA maps for dA_1, dA_{20}, and dA_2, respectively, in D_2O buffer solution, photoexcited at 266 nm. **d,e,f)** DAS obtained from global fits of the respective data sets (a,b,c), where a sequence of multiexponential decays convoluted with the experiment's instrument response function was employed as the fit function.
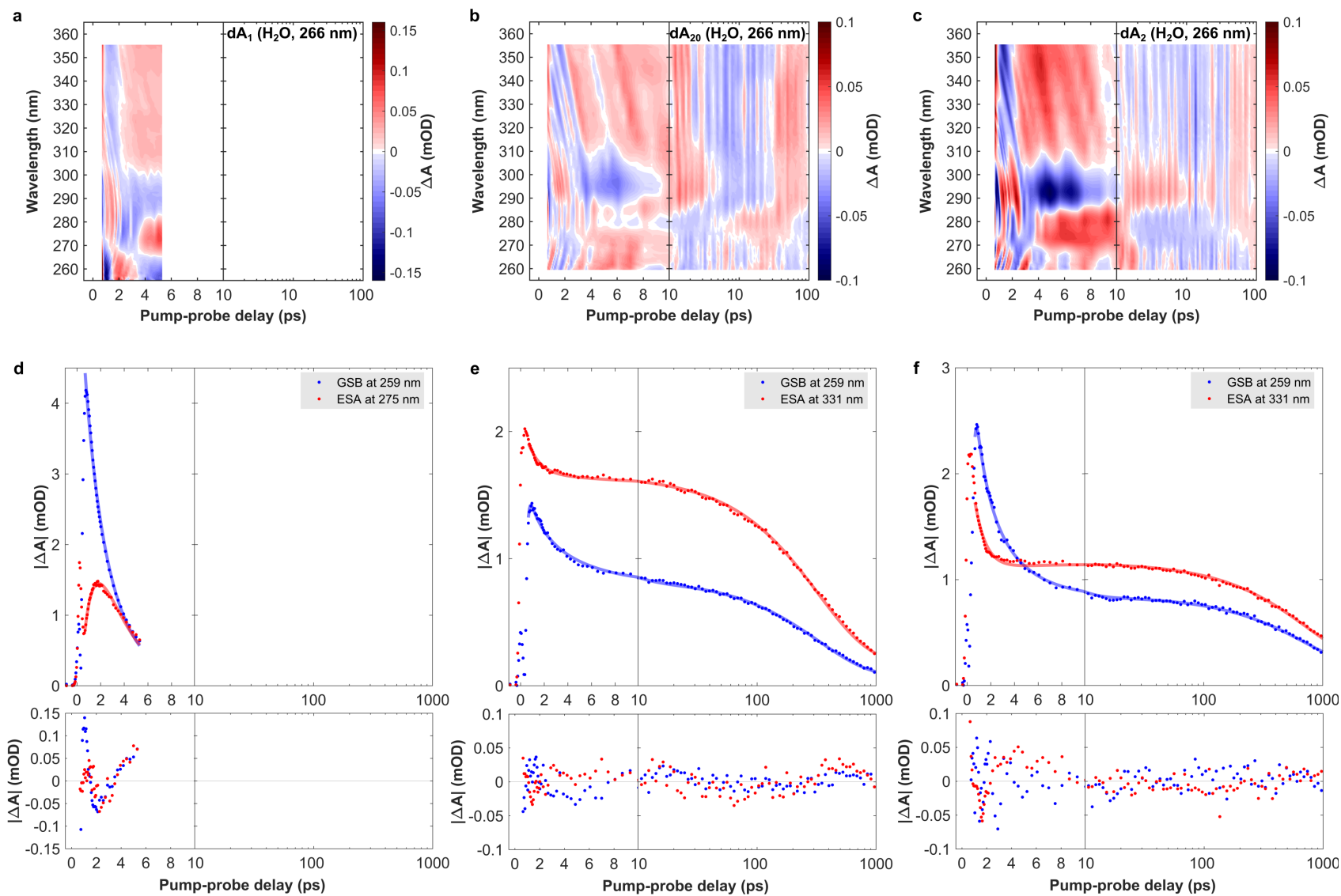
Figure 7. a,b,c) Time-wavelength maps of the residuals obtained from the fits performed on the respective data sets displayed in fig. 6. **d,e,f)** Absolute value of the TA amplitude as a function of pump-probe delay for selected probe wavelengths. Measured data points are displayed as dots and the multi-exponential fits as solid lines. The associated fit residuals are displayed in the lower panel.
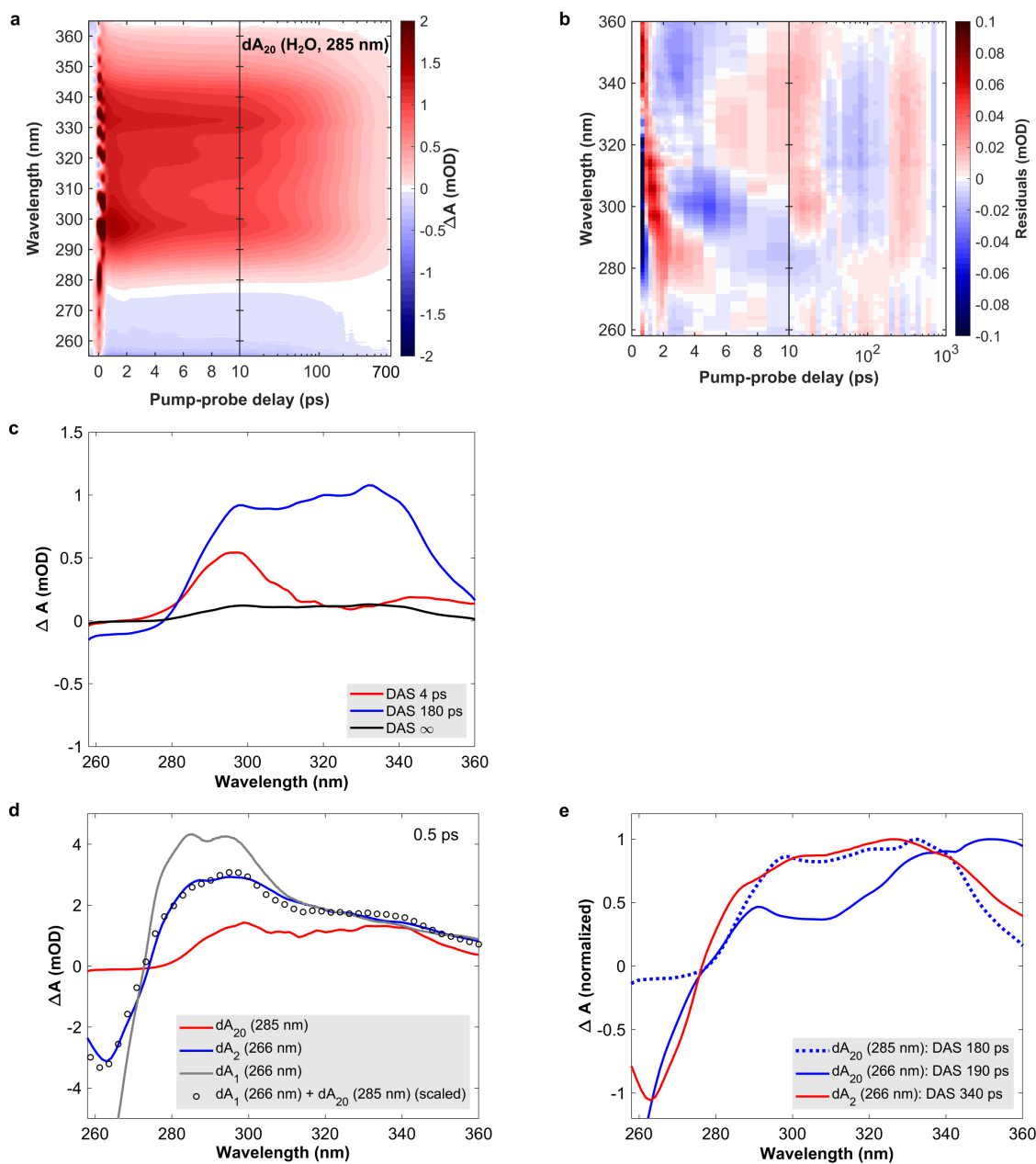
Figure 8. a,b,c) Time-wavelength maps of the residuals obtained from multi-exponential fits performed on the TA data set for dA_2 in H_2O buffer solution, photoexcited at 266 nm. To evaluate the number of exponential components required for an adequate fit, fit components were removed in a step-wise manner. Here the original fit with 4 components (a) is compared to a fit with 3 components (b), resulting in $\tau_1 \approx 0.6$ ps, $\tau_2 \approx 2.1$ ps, and $\tau_3 \approx 460$ ps, and 2 components (c), resulting in $\tau_2 \approx 2.0$ ps, and $\tau_3 \approx 490$ ps. **d,e,f)** Absolute value of the TA amplitude as a function of pump-probe delay for selected probe wavelengths. Measured data points are displayed as dots and the multi-exponential fits as solid lines. The associated fit residuals are displayed in the lower panel.

Figure 9. a) Time-wavelength TA map for dA_{20} in H_2O buffer solution, photoexcited at 285 nm. **b)** Time-wavelength map of the residuals obtained from a global fit of data set (a), where a sequence of multiexponential decays convoluted with the experiment's instrument response function was employed as the fit function. **c)** DAS obtained from the global fit of data set (a). **d)** Comparison of the TA spectra at a pump-probe delay of 0.5 ps for dA_{20} (285 nm), dA_2 (266 nm), and dA_1 (266 nm) in H_2O buffer solution. In addition the TA spectrum of dA_2 (266 nm) is compared to a sum of the TA spectra of dA_{20} (285 nm) (multiplied by 0.75) and dA_1 (266 nm) (multiplied by 0.50). The scaling factors were determined empirically. **e)** Comparison of the DAS associated with the CT exciton relaxation dA_{20} (285 nm), dA_{20} (266 nm), and dA_2 (266 nm) in H_2O buffer solution. Note that each DAS was normalized to its ESA maximum.

4 Transient absorption anisotropy

As pointed out in the Methods section, the TAA data was obtained from the same experiments that resulted in the TA data sets presented previously. For the quantitative analysis of the TAA data sets the OPTIMUS software package was then used to perform global multi-exponential fits. As the calculation of the TAA spectra involves the TA spectrum as a denominator, the TAA amplitude diverges when the TA amplitude takes values close to zero. This is the case at probe wavelengths near zero-crossings between GSB and ESA bands, at early pump-probe delays due to cross-phase modulation (see section on the IRF determination) and at late pump-probe delays where the excited state population approaches zero. For the performed global fits we accounted for all three factors by excluding probe wavelengths near zero-crossings and by excluding pump-probe delays <0.5 ps. Since each sample displayed different excited state lifetimes, the longest pump-probe delay included in the global fit was adapted accordingly. To this end, fig. 10 displays the time-wavelength TAA maps for dA_{20} (266 nm) and A_2 (266 nm) in H_2O buffer solution, along with the time-wavelength maps of the residuals obtained from the global fits. The residual maps only display non-zero values in the regions that were included in the fits, thus illustrating the chosen boundaries for each sample. Fig. 11 then displays the DAS obtained from the global fits, along with representative time traces of the TAA signal in the GSB and ESA regions of the TAA maps. For completeness, fig. 15 displays the time-wavelength TAA maps for dA_1 (266 nm) in H_2O and D_2O buffer solution. We found that for dA_{20} (266 nm) a minimum number of three exponential decays were required to fit the data. The high quality of the fit is illustrated by the low amplitude and uniform distribution of the residuals and by comparing the time trace data (dots) to the fitted curve (solid lines). Despite the good quality of the global fits, we estimated the errors of the resulting time constants to be larger than 20%. The errors were obtained by systematically varying the boundaries of the time-wavelength TAA map included in the fit and observing the variation in the fit results. In the case of dA_2 (266 nm), we found that a minimum number of two exponential decays was required to achieve a good fit of the data. In this particular case, slight mismatches of the fitted curve with the data can be observed in fig. 11d, suggesting the presence of an additional decay component. Whilst an additional decay with a time constant of approximately 50 ps can be included in the fit, we decided against this approach upon review of all other TAA data sets involving dA_2. Indeed, fitting three exponential decays to repeated experiments on dA_2 (266 nm) in H_2O and D_2O buffer solution did not converge to meaningful solutions in the majority of the obtained data sets.

Moving on, fig. 12 and fig. 13 display the TAA data sets and the results of their global analysis for dA_{20} (266 nm) and A_2 (266 nm) in D_2O buffer solution. Whilst the solvent deuteration shows a pronounced impact on the TA kinetics, a comparable effect is not observed in the TAA. Indeed, the obtained time constants mostly agree within their error ranges. Likewise, the quality of the fits is comparable to the experiments obtained in H_2O.

To check that the TAA data sets of dA_{20} in H_2O and D_2O buffer solution indeed require three

exponential decay components, we performed global fits without the intermediate component ρ_2. The obtained time traces and fit residuals are displayed in fig. 14 and show a pronounced mismatch between the data and the fit for pump-probe delays >5 ps. This confirms that three decay components are necessary to adequately fit the TAA data sets of the multimer samples.

| Sample	GSB	ESA
dA_1, H_2O, 266 nm	254 - 260 nm	296 - 306 nm
dA_2, H_2O, 266 nm	255 - 267 nm	310 - 340 nm
dA_{20}, H_2O, 266 nm	251 - 257 nm	310 - 340 nm

Table 1. Spectral boundaries for calculating the average TAA values in the GSB and ESA regions of the data sets for dA_1 (266 nm), dA_2 (266 nm), and dA_2 (266 nm) in H_2O buffer solution. The resulting time traces are displayed in fig. 4b in the main text.
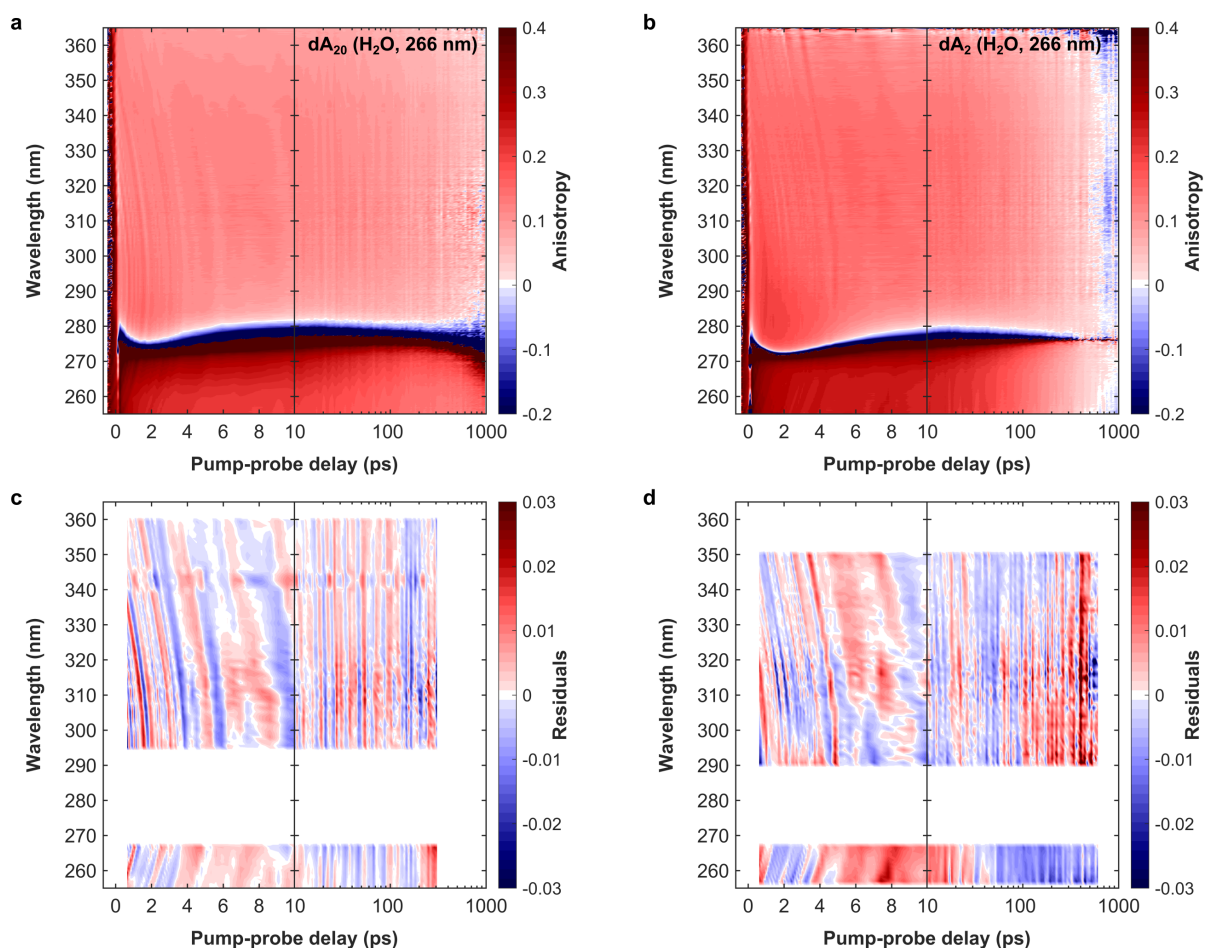

Figure 10. a,b) Time-wavelength TAA maps for dA_{20} and dA_2 in H_2O buffer solution, photoexcited at 266 nm. **c,d)** Time-wavelength maps of the residuals obtained from the global fits of the respective data sets (a,b), with details explained in the text.
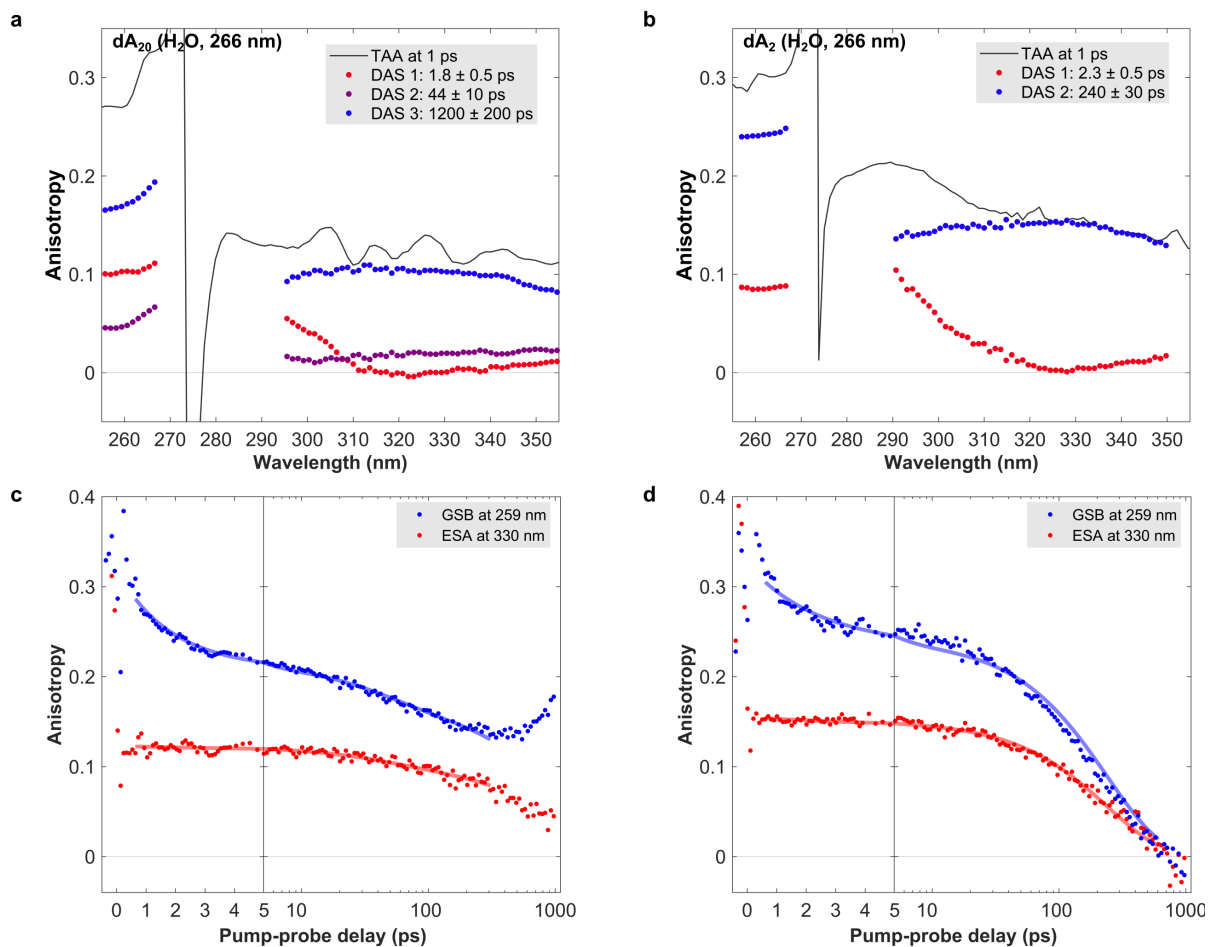
Figure 11. a,b) DAS obtained from the global fits performed on the TAA data sets for dA$_{20}$ (266 nm) and dA$_2$ (266 nm) in H$_2$O buffer solution. Note that a TAA spectrum at a pump-probe delay of 1 ps is included in order to show the amplitude and spectral width of the TAA bands in the GSB and ESA regions. **c,d)** Time traces of the TAA data (dots) in the GSB and ESA region at the spectral positions indicated in the figure legend. The solid lines show the fitted curves obtained from the global fits for a visual comparison with the data.
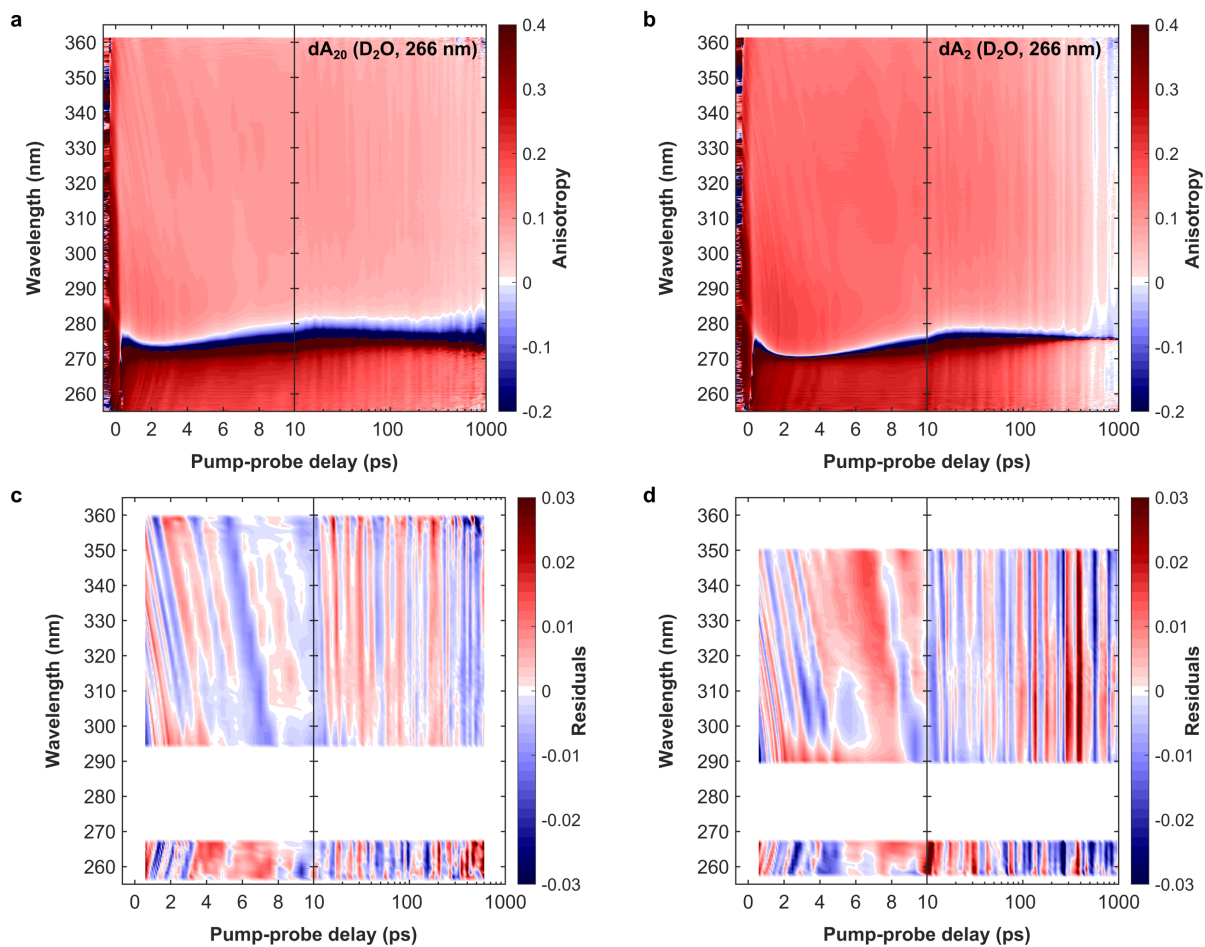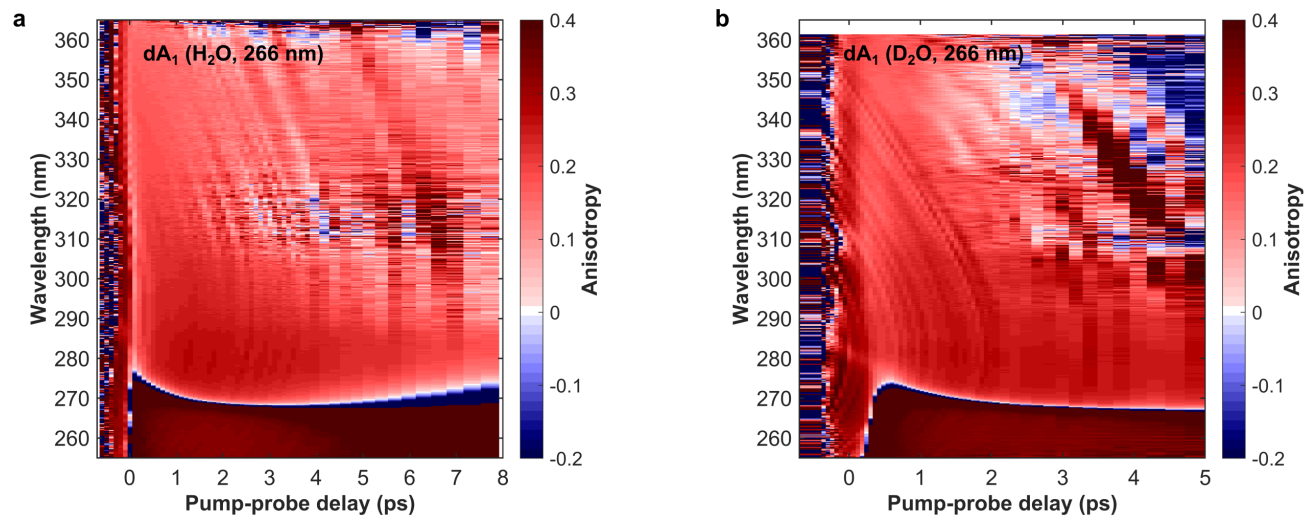
Figure 12. a,b) Time-wavelength TAA maps for dA_{20} and dA_2 in D_2O buffer solution, photoexcited at 266 nm. **c,d)** Time-wavelength maps of the residuals obtained from global fits of the respective data sets (a,b), with details explained in the text.
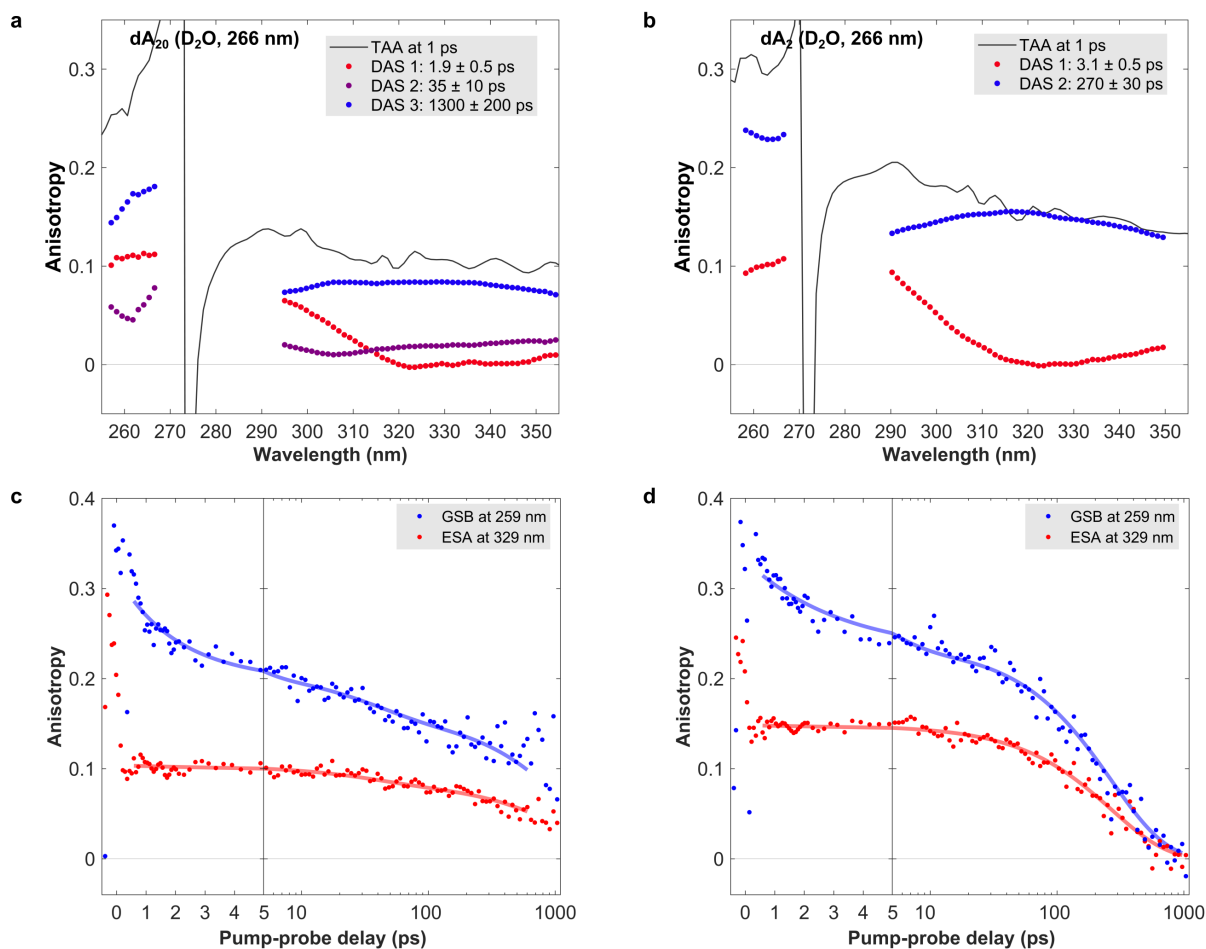
Figure 13. a,b) DAS obtained from the global fits performed on the TAA data sets for dA_{20} (266 nm) and dA_2 (266 nm) in D_2O buffer solution. Note that a TAA spectrum at a pump-probe delay of 1 ps is included in order to show the amplitude and spectral width of the TAA bands in the GSB and ESA regions. **c,d)** Time traces of the TAA data (dots) in the GSB and ESA region at the spectral positions indicated in the figure legend. The solid lines show the fitted curves obtained from the global fits for a visual comparison with the data.
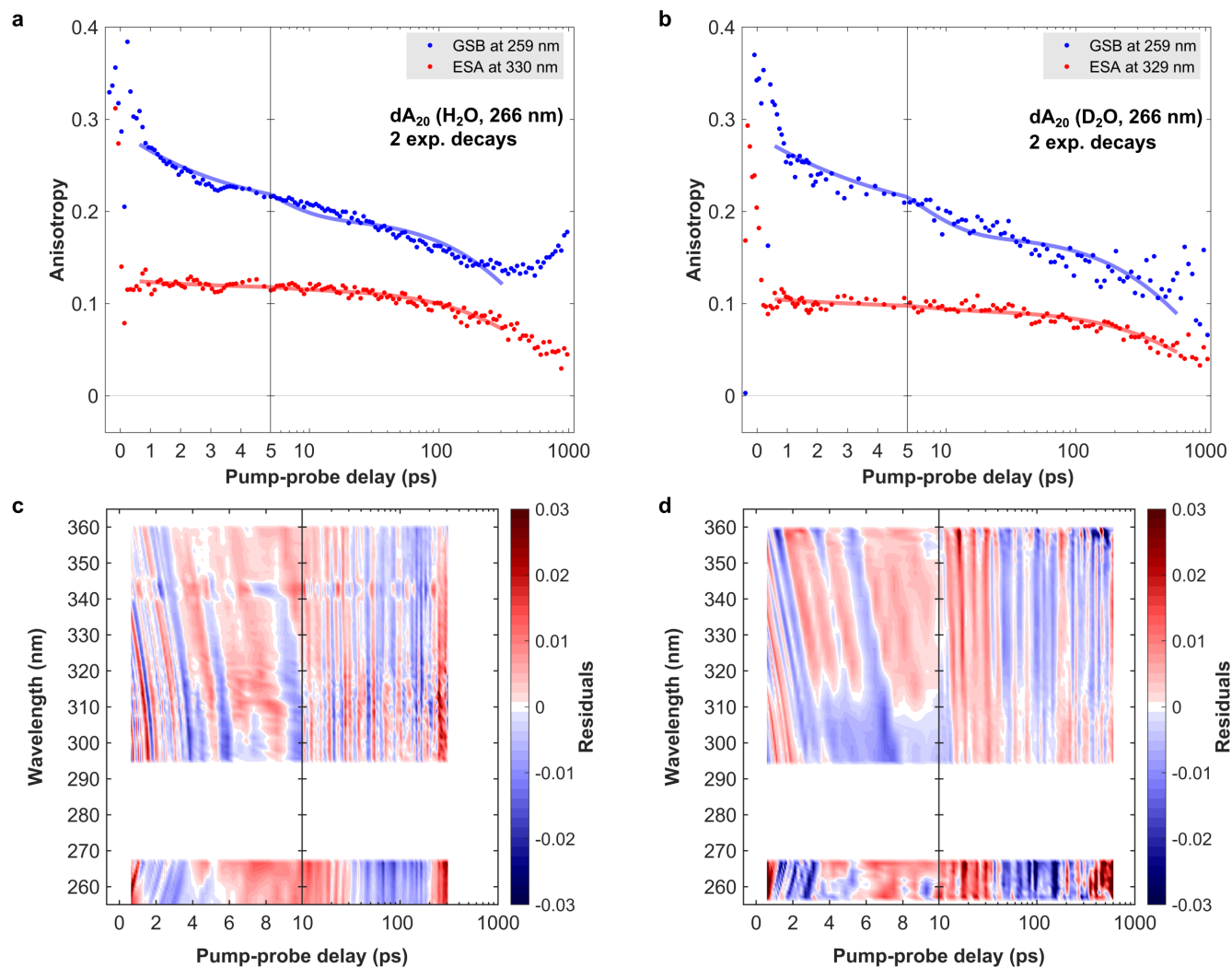
Figure 14. Evaluation of the number of fit components required for the TAA data sets of dA_{20} (266 nm) in H_2O (left panels) and D_2O buffer solution (right panels). In both cases the intermediate decay component ρ_2 was removed from the global fit. Time traces of the TAA data (dots) in the GSB and ESA region at the spectral positions indicated in the figure legend. The solid lines show the fitted curves obtained from the global fits for a visual comparison with the data. The obtained decay constants are $\rho_1 \approx 3.8$ ps and $\rho_3 \approx 650$ ps in H_2O (a) and $\rho_1 \approx 5.3$ ps and $\rho_3 \approx 890$ ps in D_2O (b). **c,d** Time-wavelength maps of the residuals obtained from the global fits of the respective data sets (a,b)

Figure 15. a,b) Time-wavelength TAA maps for dA_1 in H_2O and D_2O buffer solution, photoexcited at 266 nm.

References

1. Slavov, C., Hartmann, H. & Wachtveitl, J. Implementation and Evaluation of Data Analysis Strategies for Time-Resolved Optical Spectroscopy. *Anal. Chem.* **87**, 2328–2336, DOI: 10.1021/ac504348h (2015).

2. Takaya, T., Su, C., de La Harpe, K., Crespo-Hernández, C. E. & Kohler, B. UV excitation of single DNA and RNA strands produces high yields of exciplex states between two stacked bases. *Proc. Natl. Acad. Sci.* **105**, 10285–10290 (2008).

3. Su, C., Middleton, C. T. & Kohler, B. Base-Stacking Disorder and Excited-State Dynamics in Single-Stranded Adenine Homo-oligonucleotides. *The J. Phys. Chem. B* **116**, 10266–10274, DOI: 10.1021/jp305350t (2012).

4. Banyasz, A., Ketola, T.-M., Muñoz-Losa, A., Rishi, S., Adhikary, A., Sevilla, M. D., Martinez-Fernandez, L., Improta, R. & Markovitsi, D. UV-Induced Adenine Radicals Induced in DNA A-Tracts: Spectral and Dynamical Characterization. *The J. Phys. Chem. Lett.* **7**, 3949–3953, DOI: 10.1021/acs.jpclett.6b01831 (2016).